

The bathtub vortex in a rotating container

By A. ANDERSEN¹, T. BOHR², B. STENUM³,
J. JUUL RASMUSSEN³ AND B. LAUTRUP⁴

¹Cornell University, Department of Theoretical and Applied Mechanics, Ithaca, NY 14853, USA

²The Technical University of Denmark, Department of Physics, DK-2800 Kgs. Lyngby, Denmark

³Risø National Laboratory, Optics and Plasma Research Department, DK-4000 Roskilde, Denmark

⁴The Niels Bohr Institute, Blegdamsvej 17, DK-2100 Copenhagen Ø, Denmark

(Received 15 June 2004 and in revised form 2 November 2005)

We study the time-independent free-surface flow which forms when a fluid drains out of a container, a so-called bathtub vortex. We focus on the bathtub vortex in a rotating container and describe the free-surface shape and the complex flow structure using photographs of the free surface, flow visualizations, and velocity measurements. We find that the velocity field in the bulk of the fluid agrees with predictions from linear Ekman theory for the boundary layer at the bottom, and we discuss the limitations of linear Ekman theory for the source–sink flow in the experiment. We introduce a radial expansion approximation of the central vortex core and reduce the model to a single first-order equation. We solve the equation numerically and find that the axial velocity depends linearly on height whereas the azimuthal velocity is almost independent of height. We discuss the model of the bathtub vortex introduced by Lundgren (*J. Fluid Mech.* vol. 155, 1985, p. 381) and compare it with our experiment. We find that the measured velocities and surface profiles are described well by the model when Ekman upflow and surface tension effects are included.

1. Introduction

Flows with a free surface are abundant in nature and technological applications and occur in, e.g., jets, rivers, and the oceans. The deformation of the free surface and the underlying flow are linked to each other, and intuitively one makes such a link when looking at, e.g., the small localized surface depressions on a river and associating them with vortex structures in the water. An important example of a vortex flow with a strongly deformed free surface is the so-called bathtub vortex, which forms when a fluid drains out of a container. We present an experimental and theoretical investigation of the bathtub vortex in a rotating flow. The experiment is carried out in a water-filled cylindrical container rotating about its vertical axis of symmetry. At the centre of the bottom of the container we have a small drain-hole and we establish a time-independent flow by recirculating the water through a rotationally symmetric inlet at the cylinder wall close to the bottom. In this source–sink flow an intense central vortex with localized axial downflow is created and the free surface of the water above the drain-hole is strongly deformed and has a needle-like shape.

Bathtub vortex flows are familiar to most people, and since the free-surface depression above the drain-hole makes the presence of the vortex easily visible, it is a beautiful example of a fluid vortex (Lugt 1995). One would thus expect to find the phenomenon discussed in many fluid mechanics textbooks, whereas very few

theoretical discussions of bathtub vortex flows appear in the literature. Lamb (1945) describes a vortex with a free surface and models the flow as an outer line vortex with a viscous core, and similarly Feynman, Leighton & Sands (1965) present a simple ideal-fluid model of the bathtub vortex. They, however, neglect the downward flow, and they do not take the kinematic boundary condition at the surface into account. Donaldson & Sullivan (1960) and Lewellen (1962) discuss classes of solutions of the Navier–Stokes equations as models of bathtub vortex flows, but only for flows without a free surface. Einstein & Li (1951) model the bathtub vortex with a free surface, but they do not describe the interplay between the localized vorticity and the strong axial downflow. In the following we focus on the time-independent bathtub vortex in a rotating container. We shall not discuss the central vortex in source–sink flows in non-rotating systems as investigated experimentally by Kawakubo *et al.* (1978) or the effect of the background rotation of the Earth on the direction of rotation of the bathtub vortex (Shapiro 1962; Trefethen *et al.* 1965).

The flow structure of the bathtub vortex in a rotating container is complex with several distinct flow regions. Based on our experimental observations we first discuss the flow qualitatively and present photographs of the free surface and flow visualizations. Our goal in the paper is to provide basic theoretical understanding of the bathtub vortex in a rotating container, and to compare it with velocity and surface shape measurements. The central vortex core with localized axial downflow is surrounded by a bulk region with a two-dimensional line vortex flow which is independent of height. At the container bottom an Ekman boundary layer is formed which gives rise to upflow immediately outside the central region. We discuss the Ekman boundary layer theoretically and compare the theoretical predictions with measured flow velocities.

The most fascinating feature of the bathtub vortex is the central needle-like surface depression and the associated vortex flow, which is also the most difficult aspect of the bathtub vortex to describe theoretically. We discuss and apply the method of Lundgren (1985) for describing the central free-surface depression. Lundgren showed that with certain assumptions the Navier–Stokes equations reduce to a system of two ordinary differential equations for the azimuthal velocity and the surface height, respectively. We discuss the assumptions made by Lundgren and show that a set of weaker assumptions is sufficient for the model to apply. We find that numerical solutions of Lundgren’s equations qualitatively have the same dependence on the rotation rate of the container as the measured surface profiles when Ekman upflow from the bottom boundary layer is taken into account. We show further that surface tension effects must be included in a quantitative description of the experiment, and we compare the measured surface and velocity profiles with numerical solutions of Lundgren’s model with surface tension. A short presentation of some of our main results appeared in Andersen *et al.* (2003).

2. Experiment

2.1. Experimental setup

The present experiment was carried out in a cylindrical container on a rotating table. The setup is sketched in figure 1. The container consisted of a cylinder of radius 20 cm mounted inside a square reservoir container 0.5 cm above the plane horizontal bottom of the reservoir. The sides of both the reservoir container and the cylinder were made of transparent Perspex. A circular drain-hole of radius 0.1 cm was made in the 0.5 cm thick bottom metal plate at the centre of the cylinder. The reservoir container was

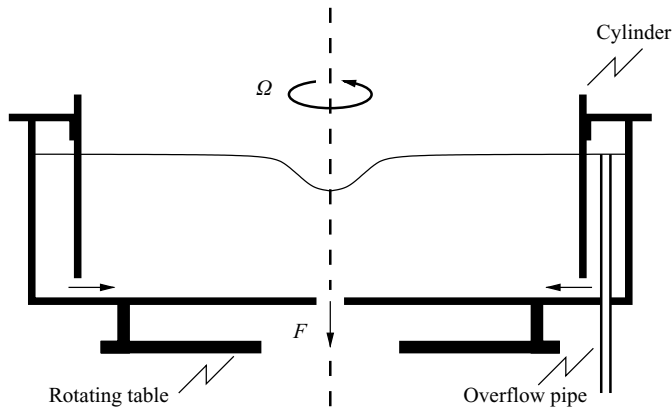


FIGURE 1. Apparatus (not to scale). The cylinder with radius 20 cm is mounted 0.5 cm above the bottom plate inside the square reservoir container which is filled with water. The container is placed on a table rotating with angular velocity Ω . The water which leaves the drain-hole with the flow rate F is pumped back into the square container outside the cylinder. The overflow pipe outside the cylinder determines the unperturbed water depth.

filled with water which entered the cylinder through the spacing between the bottom plate and the cylinder and flowed out through the drain-hole at the centre. The water which left the drain-hole driven by gravity was pumped back into the reservoir, and the water level in the container was controlled by an overflow pipe in the reservoir outside the cylinder. A transparent Perspex lid was placed on top of the cylinder several centimetres above the free surface to prevent contamination of the water. The container was rotated with a constant rotation rate about the vertical axis of symmetry of the cylinder. In this way a time-independent and rotationally symmetric free-surface flow was established with a well-defined rotation rate of the container and a well-defined free-surface height at the cylinder wall. The free-surface shape and the velocity field of the time-independent flow were measured at rotation rates of 6 r.p.m. (rotations per minute), 12 r.p.m., and 18 r.p.m. after a spin-up time of 1200 s. The free-surface height close to the cylinder wall was 10.9 cm in all three cases.

2.2. Free surface

Figure 2 shows the observed profiles of the free surface for the time-independent flow at rotation rates of 6 r.p.m., 12 r.p.m., and 18 r.p.m. In the experiment we held the radius of the drain-hole and the unperturbed fluid depth constant, while we varied the rotation rate of the container. The depth of the dip in the free surface increases with increasing rotation rate, whereas the radius of the central region, where the dip is very distinct, is almost unaltered. Using a setup similar to the one sketched in figure 1 with fixed unperturbed fluid depth, but with container radius 10 cm instead of 20 cm and with a variable radius of the drain-hole, we observed that the depth of the central depression depended sensitively on the radius of the drain-hole and less on the rotation rate of the container. The outflow is driven by gravity and the flow rate through the drain-hole is thus approximately constant when both the unperturbed fluid depth and the radius of the drain-hole are kept constant. A straightforward application of Torricelli's theorem (Batchelor 1967) overestimates the measured flow rate by 20 % when the container is not rotating. The measured flow rate, F , decreases by approximately 15 % when the rotation rate, $\Omega/2\pi$, is increased from 6 r.p.m. to 18 r.p.m. as shown in table 1.

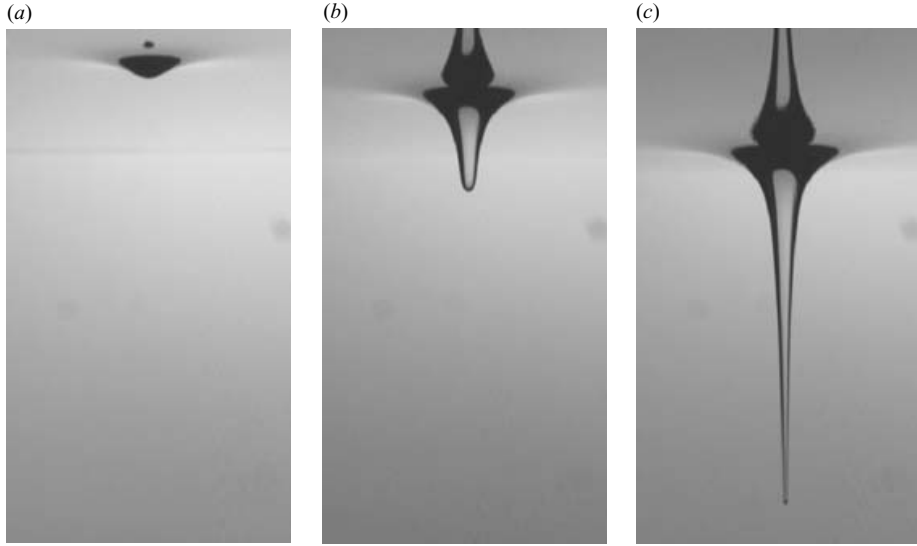


FIGURE 2. The free-surface dip depends sensitively on the rotation rate of the container. Picture (a) was taken at 6 r.p.m. (rotations per minute), (b) at 12 r.p.m., and (c) at 18 r.p.m. In each photograph the area is 4.0 cm (horizontally) \times 7.2 cm (vertically) and the lower edge of the frame is 4.2 cm above the drain-hole. The structure above the surface is due to reflections.

$\Omega/2\pi$ (r.p.m.)	F (cm ³ s ⁻¹)	Ro	$Ek(10^{-5})$	$\Omega_C/2\pi(10^4$ r.p.m.)	Ro_C
6	3.62	0.019	1.8	0.9	0.014
12	3.54	0.013	0.9	1.3	0.010
18	3.16	0.010	0.6	1.4	0.009

TABLE 1. Rotation rate of the container, Ω , measured flow rate, F , global Rossby number based on the flow in the bottom Ekman layer, $Ro = F/2\pi\sqrt{\nu\Omega}L^2$, global Ekman number, $Ek = \nu/2\Omega L^2$, estimate of the central rotation rate, $\Omega_C = F/\pi\sqrt{\nu/\Omega}R_0^2$, and central Rossby number based on the velocity of the central downflow, $Ro_C = W/H\Omega_C$.

2.3. Tip instability

The tip of the free-surface dip is stable when the rotation rate of the container is below a certain value. At higher rotation rates the dip is deeper and the tip oscillates vertically, and at even higher rotation rates air bubbles detach from the tip as shown in figure 3. Initially the bubbles are not spherical but appear elongated. Further downstream they attain an almost spherical shape. When the rotation rate of the container is increased further, both the central surface depression and the frequency of bubble shedding increases until the air-filled core extends all the way down through the drain-hole.

Around the critical value of the rotation rate (which is approximately 22 r.p.m.) the dip appears almost like a cylinder of air surrounded by rapidly spinning water. The radius of the air cylinder is about 0.05 cm. This length scale is smaller than the capillary length and the bubble-forming instability is induced by surface tension. However, the linear stability of a rotating, cylindrical, and hollow jet with surface tension is increased by increasing the rotation rate (Ponstein 1959; Pedley 1967). We therefore speculate that the axial downflow should be included to model the

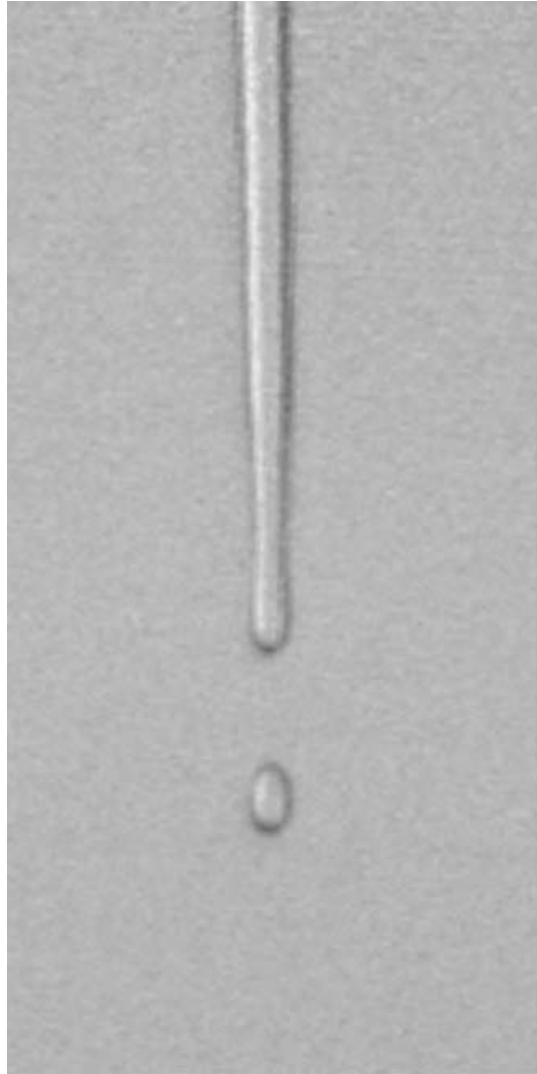


FIGURE 3. The tip of the surface depression is unstable when the rotation rate of the container is high. An air bubble with radius of about 0.05 cm has just detached from the tip and is dragged down the drain-hole by the surrounding flow. The photograph was taken with a setup similar to the one sketched in figure 1, but with container radius equal to 10 cm instead of 20 cm.

instability and that the instability sets in at a critical value of the rotation rate when the downward drag becomes sufficiently large to overcome the buoyancy of the bubbles formed by the capillary instability and drag the bubbles downward. An estimate based on this argument agrees well with the measured critical value of the rotation rate (Andersen *et al.* 2003), but detailed measurements of the flow field around the tip of the surface depression are needed to verify the proposed instability mechanism. We note that the periodic shedding of bubbles at the tip resembles the generation of monodisperse bubbles in microchannels using a so-called flow-focusing device (Garstecki *et al.* 2004), and we speculate that the instabilities in the two systems are of similar type.

2.4. Flow structure

Figures 4 and 5 show flow visualizations made at 12 r.p.m. by illuminating a vertical cross-section through the axis of symmetry and then adding fluorescent dye at the surface (figure 4) or at the bottom inlet (figure 5). The fluorescent dye was only visible when illuminated by the vertical light sheet created using a slide projector with a thin metal plate with a slit in front of it. Figure 4 shows the downflow above the drain-hole. The dye was added at the surface some distance from the centre and is flowing toward the centre in a thin surface boundary layer. The small free-surface dip (see also figure 2*b*) is visible above the central localized downflow region which appears like a ‘drainpipe’ with radius comparable to that of the drain-hole. The free-surface boundary layer carries only a small fraction of the total flow rate, and most of the inflow takes place in the bottom boundary layer.

The photographs in figure 5 show a time series of visualizations using dye added at the bottom inlet. Outside the central region the flow is controlled by the rotation of the container, and the boundary layer at the bottom has the characteristics of an Ekman layer, i.e. a boundary layer in a rotating flow at a free or solid boundary which is normal to the axis of rotation. The thickness of the Ekman layer is almost constant, and the flow in the so-called geostrophic bulk above it is two-dimensional and independent of height as expressed in the Taylor–Proudman theorem, which is valid when the Coriolis terms in the governing equations dominate over nonlinear and viscous effects (Batchelor 1967). At 12 r.p.m. the Ekman layer thickness is about 0.1 cm. The Ekman layer is visible to the left in figure 5(*a*) and immediately to the right of the drain-hole in figure 5(*b*). The blob of dye spirals upward around the axis of symmetry and forms the layered structure in figure 5(*c–f*) which surrounds the downflow ‘drainpipe’ from the free-surface layer. We note that a similar upflow was visualized by Lewellen (1962) close to the drain-hole in a rotating flow without a free surface. The mechanism which creates the upflow is similar to Ekman pumping, i.e. upflow due to a vortical flow above a rotating bottom boundary (Batchelor 1967). However, standard linear Ekman theory does not apply in the central region and the nonlinear terms in the boundary layer equations must be included to model the bottom boundary layer close to the drain-hole.

Figure 6 shows the long path followed by a small tracer particle which spirals upward from the Ekman layer and then down toward the drain-hole. The recording was made with a vertical light sheet as in the flow visualizations and the trajectory was identified using particle tracking software (DigImage, University of Cambridge, UK).

Figure 7 summarizes our qualitative description of the flow structure by showing the various flow regions and a sketch of the cross-section through the spiralling streamlines.

2.5. Estimates of the central rotation rate and the depth of the free surface dip

We conclude the phenomenological discussion of the bathtub vortex by estimating the central rotation rate, Ω_C , and the depth of the central surface depression, Δh . In addition we provide a table summarizing the non-dimensional parameters describing the various flow regions. In §3 we show that the flow in the bulk of the fluid is a line vortex with strength related to the total flow rate, F , and the thickness of the bottom Ekman layer, $\delta = \sqrt{\nu/\Omega}$, where ν is the kinematic viscosity of the fluid and Ω is the rotation rate of the container. We assume that the central vortex has a rigidly rotating core with radius equal to the radius of the drain-hole, R_0 , and by matching

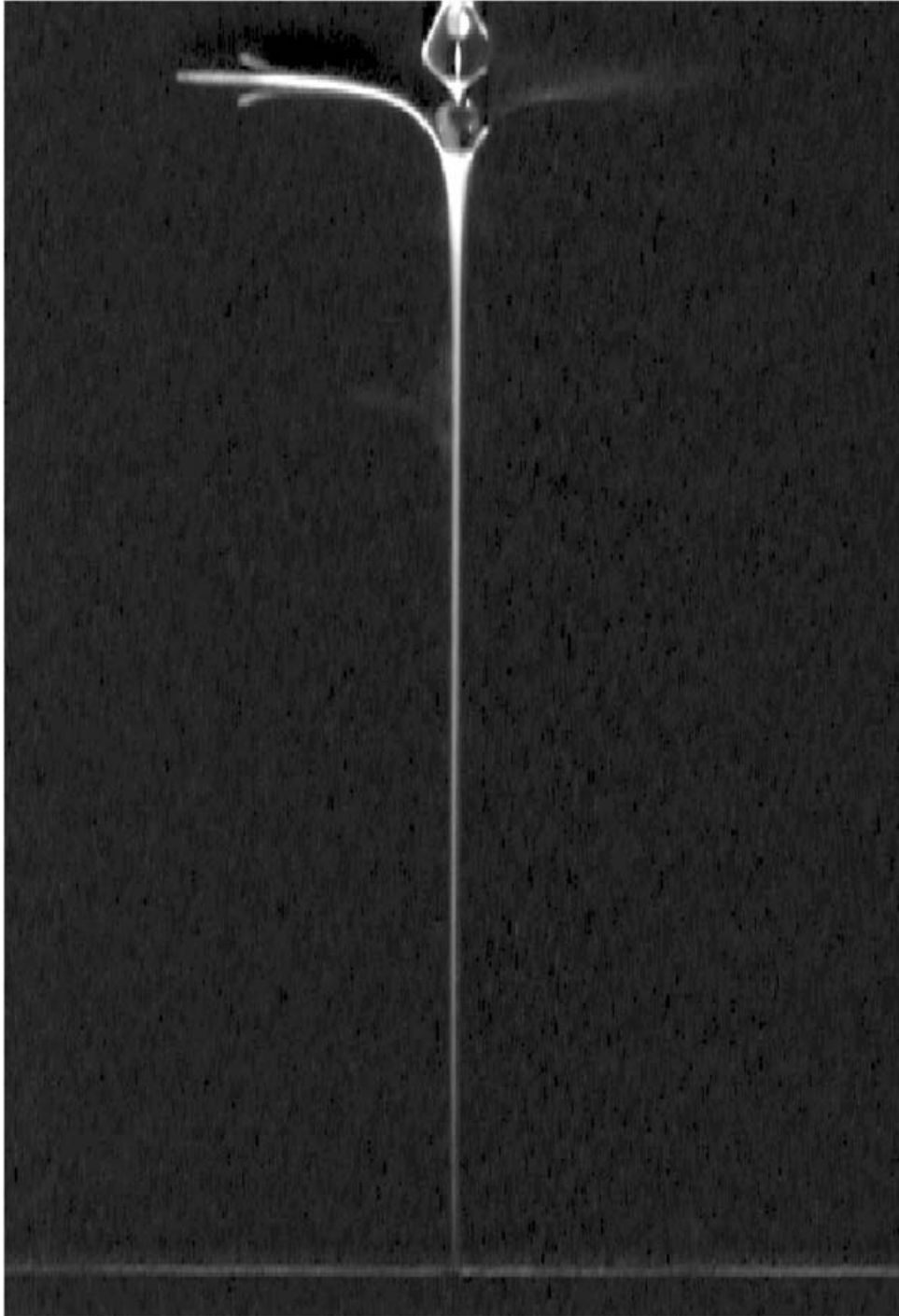


FIGURE 4. Visualization of the downflow in the vortex core above the drain-hole at 12 r.p.m. The dye was added at the surface and is flowing in a free-surface boundary layer to the core region where it flows rapidly downward to the drain-hole. The top part of the image shows reflections in the free surface which are artifacts of the method of observation.

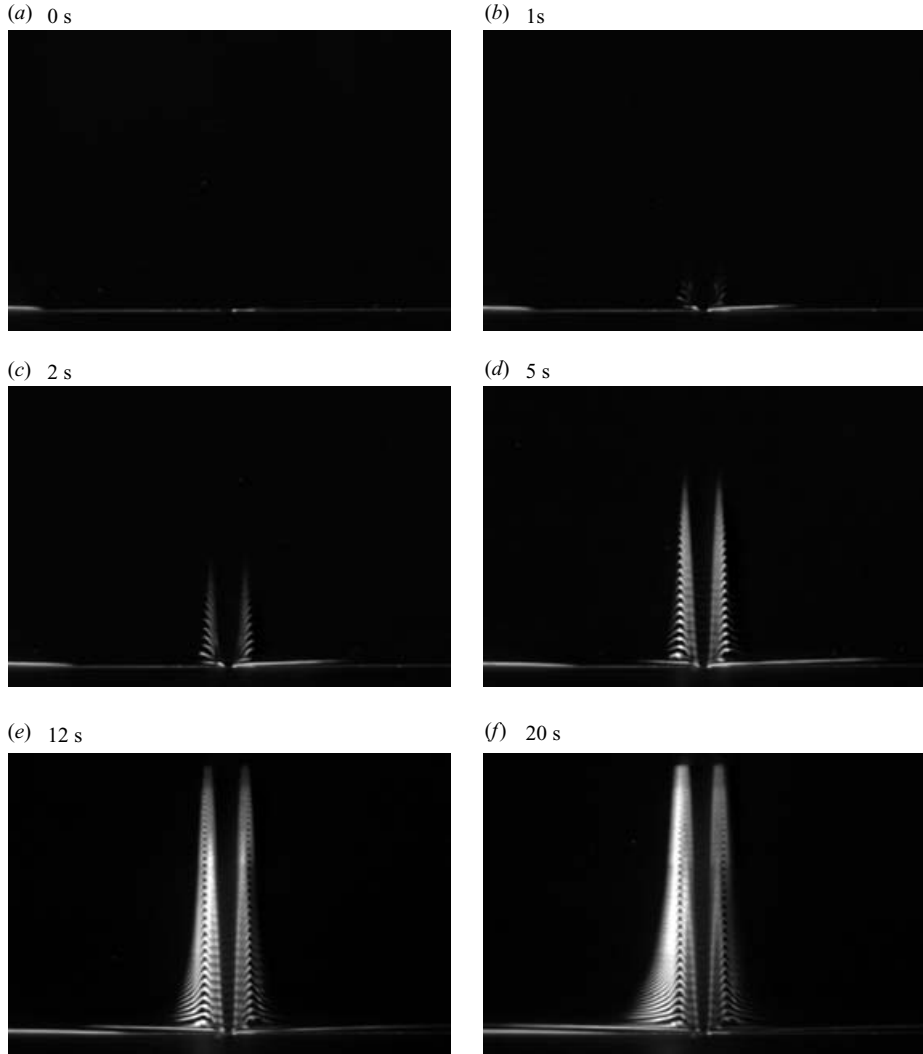


FIGURE 5. Time series of visualizations of the flow in the bottom boundary layer and the central upflow around the drain-hole at 12 r.p.m. The images are 7.8 cm (horizontally) \times 5.4 cm (vertically) with the bottom visible as the thin bright line. The bottom Ekman boundary layer is about 0.1 cm thick and initially visible to the left of the drain-hole in (a). Subsequently, some of the dye from the Ekman layer goes directly down the drain, whereas the rest of the dye spirals upward around the axis of symmetry until the flow turns and the dye spirals down toward the drain-hole.

the solutions we find

$$\Omega_C = \frac{F}{\pi \sqrt{\nu/\Omega} R_0^2}, \tag{2.1}$$

which gives $\Omega_C \approx 10^4$ r.p.m., i.e. a central rotation rate that is three orders of magnitude larger than the rotation rate of the container as summarized in table 1.

Neglecting surface tension and assuming that most of the surface variation takes place for $r < R_0$ where the surface is roughly parabolic, the order of magnitude of

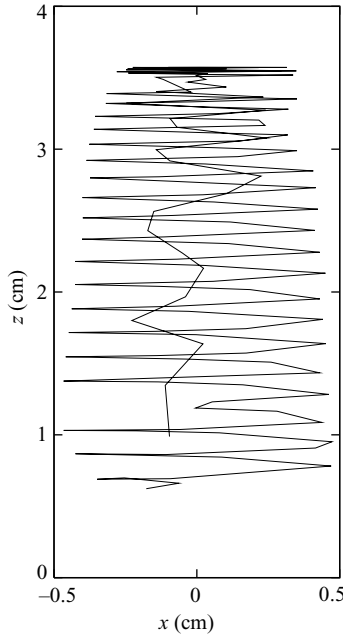


FIGURE 6. The trajectory of a tracer particle at 6 r.p.m. The tracer particle spirals upward at a distance between 0.4 cm and 0.5 cm from the centre until it turns at a height of 3.6 cm above the bottom and spirals down toward the drain-hole with increasing vertical velocity.

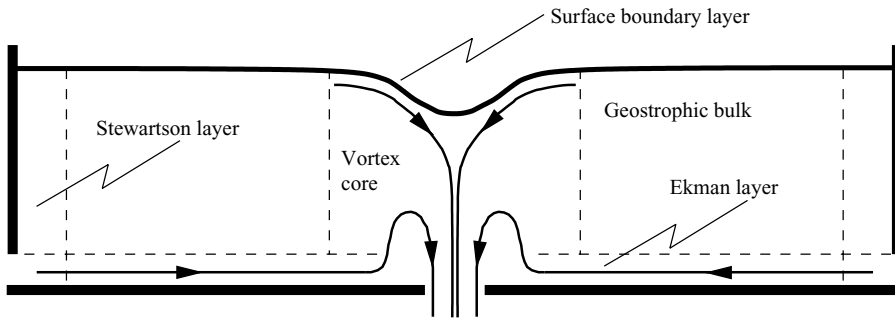


FIGURE 7. The characteristic flow regions of the bathtub vortex. The main part of the radial in-flow is carried by the bottom Ekman boundary layer, and the upwelling region next to the central region surrounds the central drainpipe from the free surface above the drain-hole.

the depth of the central surface depression, Δh , is given by the expression

$$\Delta h = \frac{\Omega_c^2 R_0^2}{2g} = \frac{F^2 \Omega}{2\pi^2 g \nu R_0^2}, \quad (2.2)$$

where g is the acceleration due to gravity. The simple estimate of Δh suggests that the depth of the central surface depression depends more sensitively on F than on Ω , and also that Δh should increase if ν is decreased, e.g. by increasing the temperature. With the measured flow rates we estimate Δh to be 5 cm at 6 r.p.m. and 11 cm at 18 r.p.m., whereas the measured values are 0.2 cm at 6 r.p.m. and 4.8 cm at 18 r.p.m.

We overestimate Δh mainly because we have neglected surface tension which will reduce the depth of the central depression by an amount proportional to the product of the surface tension, α , and the central surface curvature, $\kappa(0)$. Assuming that $\kappa(0) \approx 2/R_0$ we estimate that surface tension will reduce the depth of the central dip by $2\alpha/(g\rho R_0) \approx 1$ cm, where ρ is the density of the fluid. It is therefore clear that surface tension must be taken into account in a quantitative description of the bathtub vortex as we discuss in §5.

3. The Ekman boundary layer at the bottom

3.1. Governing equations and non-dimensional numbers

The Navier–Stokes equations and the continuity equation for a time-independent and incompressible flow in the reference frame co-rotating with the container are

$$(\mathbf{u} \cdot \nabla)\mathbf{u} = -\frac{1}{\rho}\nabla p + \nu\nabla^2\mathbf{u} - 2\boldsymbol{\Omega} \times \mathbf{u}, \quad (3.1)$$

$$\nabla \cdot \mathbf{u} = 0, \quad (3.2)$$

where \mathbf{u} is the velocity in the co-rotating reference frame, p the effective pressure which includes a gravitational and a centrifugal term, $\boldsymbol{\Omega}$ the angular velocity of the container, ρ the fluid density, and ν the kinematic viscosity.

The characteristic value of the ratio between the nonlinear term and the Coriolis term is the Rossby number, Ro , and the characteristic value of the ratio between the viscous term and the Coriolis term is the Ekman number, Ek . We use the definitions

$$Ro = \frac{U}{2\Omega L}, \quad (3.3)$$

$$Ek = \frac{\nu}{2\Omega L^2}, \quad (3.4)$$

where L is the characteristic length scale and U is the characteristic velocity scale (see also table 1). In linear Ekman theory the Rossby number is assumed to be small, and thus the nonlinear terms in the Navier–Stokes equations are neglected.

3.2. Linear Ekman theory for source–sink flows

We first describe the bottom Ekman layer and the source–sink flow outside the central region, and therefore we do not include the drain-hole and the associated downflow at this point. We use polar coordinates (r, θ, z) with corresponding velocity components (u, v, w) . Similar to standard boundary layer theory only the derivatives with respect to z are kept in the viscous terms, and the Navier–Stokes equations (3.1) reduce to

$$0 = -\frac{1}{\rho}\frac{\partial p}{\partial r} + \nu\frac{\partial^2 u}{\partial z^2} + 2\Omega v, \quad (3.5)$$

$$0 = \nu\frac{\partial^2 v}{\partial z^2} - 2\Omega u, \quad (3.6)$$

$$0 = -\frac{1}{\rho}\frac{\partial p}{\partial z}. \quad (3.7)$$

Since it is assumed that the vertical velocities are small it follows from the axial Navier–Stokes equation (3.7) that the pressure is independent of z and that the pressure gradient $\partial p/\partial r$ therefore is equal to its value in the bulk of the fluid where the pressure gradient and the Coriolis force balance each other. The governing

equations thus reduce to the following set of coupled linear ordinary differential equations

$$0 = v \frac{\partial^2 u}{\partial z^2} + 2\Omega(v - v_0), \quad (3.8)$$

$$0 = v \frac{\partial^2 v}{\partial z^2} - 2\Omega u, \quad (3.9)$$

where v_0 is the azimuthal velocity in the geostrophic bulk of the fluid (Batchelor 1967). With the boundary conditions $u(r, z) = v(r, z) = 0$ at $z = 0$, $u(r, z) \rightarrow 0$ as $z \rightarrow \infty$, and $v(r, z) \rightarrow v_0(r)$ as $z \rightarrow \infty$, the equations have the solution

$$u(r, z) = -v_0(r)e^{-z/\delta} \sin(z/\delta), \quad (3.10)$$

$$v(r, z) = v_0(r)[1 - e^{-z/\delta} \cos(z/\delta)], \quad (3.11)$$

where the Ekman boundary layer thickness is defined as

$$\delta = \sqrt{\frac{\nu}{\Omega}}. \quad (3.12)$$

The thickness of the Ekman layer is thus constant in the linear approximation. The continuity equation (3.2) relates u and w in the following way

$$\frac{1}{r} \frac{\partial(ru)}{\partial r} + \frac{\partial w}{\partial z} = 0, \quad (3.13)$$

and since $w(r, z) = 0$ for $z = 0$, it follows that

$$w(r, z) = \frac{\delta}{2r} \frac{d(rv_0)}{dr} (1 - e^{-z/\delta} [\sin(z/\delta) + \cos(z/\delta)]). \quad (3.14)$$

In the bulk of the fluid above the Ekman layer, i.e. in the limit of large z , the vertical velocity component is therefore proportional to the z -component of the vorticity ω_z :

$$w_0 = \frac{\delta}{2r} \frac{d(rv_0)}{dr} = \frac{\delta}{2} \omega_z. \quad (3.15)$$

In linear Ekman theory a vortex with positive vorticity thus gives rise to Ekman pumping (upflow) whereas a vortex with negative vorticity produces Ekman suction (downflow). The bathtub vortex produces a weak upflow from the Ekman layer in the upwelling region next to the central region, whereas linear Ekman theory does not apply in the central vortex core where the rapid downflow is observed.

The bathtub vortex flow outside the central vortex core, i.e. in the bulk of the fluid, can be modelled as a line vortex flow with circulation Γ :

$$v_0(r) = \frac{\Gamma}{2\pi r}. \quad (3.16)$$

It follows from equation (3.14) that $w = 0$ in this particular solution since the flow is irrotational. This is required to satisfy the kinematic boundary condition at the almost horizontal free surface outside the vortex core. The circulation is related to the flow rate, F , which we define as the integral

$$F \equiv - \int_0^\infty dz 2\pi r u = \frac{\Gamma \delta}{2}. \quad (3.17)$$

$\Omega/2\pi(\text{r.p.m.})$	$F(\text{cm}^3\text{s}^{-1})$	$\delta(\text{mm})$	$F/\pi\delta(\text{cm}^2\text{s}^{-1})$	$A(\text{cm}^2\text{s}^{-1})$
6	3.62	1.190	9.7	10.2
12	3.54	0.842	13.4	14.2
18	3.16	0.687	14.6	16.0

TABLE 2. The measured flow rate, F , the thickness of the Ekman layer, $\delta = \sqrt{\nu/\Omega}$, and the vortex strength predicted from linear Ekman theory, $F/(\pi\delta)$, for different values of the angular velocity, Ω . The 5th column shows the values of A obtained from fits of the line vortex A/r to the measured azimuthal velocity profiles in the range $5\text{ cm} \leq r \leq 15\text{ cm}$. The theoretical predictions of the vortex strengths $F/(\pi\delta)$ agree with the measured values of A to within 5–10 %.

A particular solution of (3.8) and (3.9) modelling the bathtub vortex is therefore

$$u = -\frac{F}{\pi\delta r} e^{-z/\delta} \sin(z/\delta), \tag{3.18}$$

$$v = \frac{F}{\pi\delta r} [1 - e^{-z/\delta} \cos(z/\delta)], \tag{3.19}$$

$$w = 0. \tag{3.20}$$

Outside the vortex core in the bulk of the fluid far above the Ekman layer we thus expect that $u \approx 0$ and $v \approx F/(\pi\delta r)$ because of the special structure of the linear Ekman solution. Similar results were derived and confirmed experimentally for a source–sink flow without a free surface by Mory & Yurchenko (1993).

A source–sink vortex has a central core where the line vortex model (3.18)–(3.20) does not apply and the flow is in solid body rotation. A simple azimuthal velocity profile that describes this structure in the bulk of the fluid can be written

$$v_0(r) = \frac{F}{\pi\sqrt{\nu/\Omega} r} \left[1 - \exp\left(-\frac{r^2}{R_0^2}\right) \right], \tag{3.21}$$

where R_0 is the radius of the drain-hole. The velocity profile matches the outer line vortex (3.16) and describes a vortex core with solid body rotation. In this case linear Ekman theory (3.15) predicts the Gaussian upflow profile

$$w_0(r) = \frac{F}{\pi R_0^2} \exp\left(-\frac{r^2}{R_0^2}\right). \tag{3.22}$$

In the following paragraphs we discuss the measured azimuthal and upflow velocities.

3.3. Measured azimuthal velocity profiles

Figure 8 shows the azimuthal velocity profile measured at 6 r.p.m. in the bulk of the fluid 5.7 cm above the bottom. The flow outside the central region is that of a line vortex and at the cylinder wall a vertical boundary layer is formed. We measured similar velocity profiles at 12 r.p.m. and 18 r.p.m. Table 2 summarizes the measurements of the azimuthal velocities in the bulk of the fluid at 6 r.p.m., 12 r.p.m., and 18 r.p.m. and shows the measured total flow rate and the calculated Ekman layer thickness. We used the kinematic viscosity of water $\nu = 0.0089\text{ cm}^2\text{ s}^{-1}$ which is valid at 25 °C (Kaye & Laby 1973). The measured azimuthal velocities in the bulk are modelled well by the line vortex $v_0 = F/(\pi\delta r)$, and the theoretical values agree with the measured vortex strengths to within 5–10 %. The experiment thus confirms the prediction of linear Ekman theory.

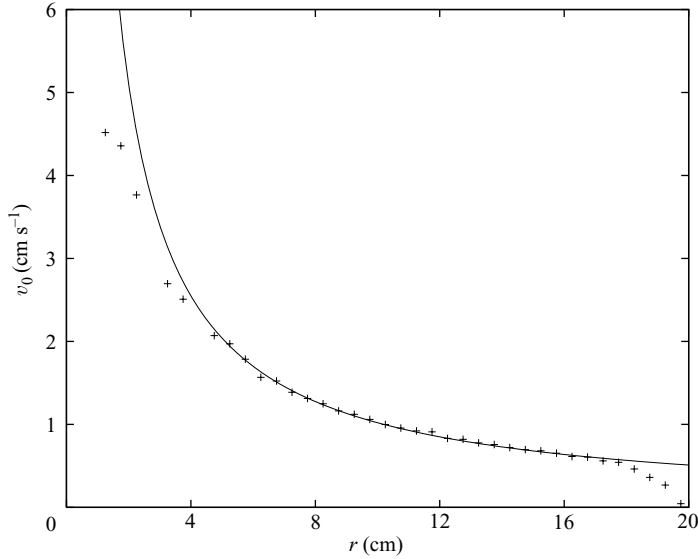


FIGURE 8. The azimuthal velocity profile measured at 6 r.p.m. using particle tracking with a horizontal light sheet and the best fit of a line vortex A/r to the experimental data. The plus signs show the measurements and the solid curve is the best fit in the range $5 \text{ cm} \leq r \leq 15 \text{ cm}$. The vertical Stewartson boundary layer at the cylinder wall is about 1 cm thick.

The vertical boundary layer at the cylinder wall is much thicker than the bottom Ekman layer. Following Greenspan (1968) we estimate that the thickness of this so-called Stewartson layer is $L Ek^{1/4} \approx 1 \text{ cm}$, where the Ekman number is defined in equation (3.4) and where we use the radius of the container $L = 20 \text{ cm}$ as the characteristic length scale. The estimated boundary layer thickness agrees with the results shown in figure 8.

3.4. Validity of the linear Ekman solution

The linear approximation (3.8) and (3.9) is only valid when the flow relative to the background rotation is weak and the nonlinear terms in the Navier–Stokes equations are negligible, i.e. when the Rossby number (3.3) and the Ekman number (3.4) are small:

$$Ro \ll 1, \quad Ek \ll 1. \tag{3.23}$$

We therefore estimate the local Rossby number and the local Ekman number:

$$Ro = \frac{F}{2\pi\sqrt{\nu\Omega}r^2}, \quad Ek = \frac{\nu}{2\Omega r^2}, \tag{3.24}$$

where we use $U \approx F/(\pi\delta r)$ and $L \approx r$. At 12 r.p.m. we obtain the estimates

$$Ro \approx 1 \quad \text{when} \quad r \approx 2 \text{ cm}, \quad Ek \approx 1 \quad \text{when} \quad r \approx 0.06 \text{ cm}. \tag{3.25}$$

The nonlinear terms are therefore important in the bathtub vortex experiment at small values of r whereas they can be neglected when modelling the flow outside the central vortex core as in the linear Ekman theory for the source–sink flow.

3.5. The upflow from the Ekman layer

In the bathtub vortex experiment the main part of the radial inflow is carried by the bottom Ekman layer, and radial inflow above the Ekman layer takes place in

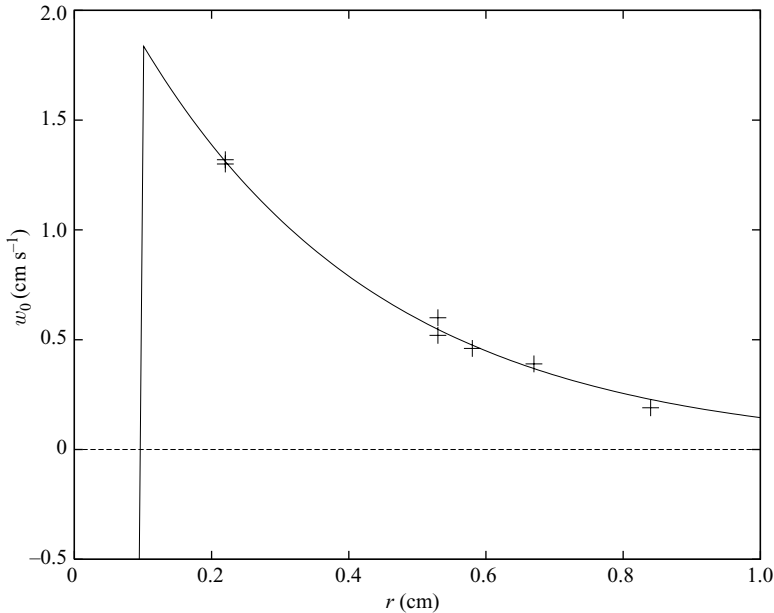


FIGURE 9. The upflow velocities above the Ekman layer at 12 r.p.m. The plus signs show upflow velocities measured 1 cm above the bottom and the solid curve a fit to the experimental data outside the drain-hole using the profile (3.27) with $C = 2.5 \text{ cm s}^{-1}$ and $d = 0.35 \text{ cm}$.

the central region where upflow from the bottom layer supplies fluid through Ekman pumping. To model the vertical velocity above the Ekman layer, w_0 , we therefore require that the sum of the upflow from the Ekman layer and the central downflow to be zero

$$0 = \int_0^\infty w_0(r) 2\pi r \, dr. \tag{3.26}$$

The dye visualization of the bottom flow in figure 5 shows that the maximum upflow velocity above the bottom Ekman layer is approximately 1 cm s^{-1} , and vertical velocities measured using particle tracking with a vertical light sheet suggest that the upflow w_0 decreases exponentially with increasing r .

Figure 9 shows measured upflow velocities 1 cm above the bottom at 12 r.p.m. and a theoretical fit of the form

$$w_0(r) = C e^{-r/d}, \tag{3.27}$$

where C and d are constants. In linear Ekman theory the length scale for the upflow is given by the radius of the vortex core as shown in equations (3.21) and (3.22), and in the nonlinear case we therefore expect the length scale, d , to be comparable with the radius of the vortex core. In a theoretical analysis of the nonlinear Ekman equations using an averaging method (Andersen, Lautrup & Bohr 2003) we found that nonlinear effects make the profile slightly wider than the prediction of linear Ekman theory. These results support the value $d = 0.35 \text{ cm}$ measured in the bathtub vortex experiment.

Outside the downflow region we use the exponential profile and for simplicity we assume that the downflow inside the drain-hole is a plug flow

$$w_0(r) = \begin{cases} -\frac{Q}{\pi R^2} & \text{if } r \leq R \\ \frac{Q}{2\pi d(R+d)} \exp\left(-\frac{r-R}{d}\right) & \text{if } r > R, \end{cases} \quad (3.28)$$

where R is the radius of the downflow region, Q is the part of the total flow rate F which flows upward because of Ekman pumping outside the downflow region, and the prefactors for $r \leq R$ and $r > R$ are related by equation (3.26).

We have only a few data points for the downward velocities in the central region at 12 r.p.m., and we are therefore not able to determine the profile of the downward flow in detail. For simplicity we use the plug-flow profile. The actual profile is most likely in between a parabolic profile and the plug-flow profile. Our measurements show that the downward flow is not confined within a radius of 0.1 cm. At 12 r.p.m. we find that $w_0(r = 0.013 \text{ cm}) = -84.7 \text{ cm s}^{-1}$, $w_0(r = 0.080 \text{ cm}) = -52.6 \text{ cm s}^{-1}$, and $w_0(r = 0.130 \text{ cm}) = -21.0 \text{ cm s}^{-1}$. The actual radius of the drainpipe 1 cm above the bottom is therefore between 0.1 cm and 0.2 cm, and immediately above the Ekman layer the drainpipe contracts substantially as it approaches the drain-hole. In the following we use a value of R between 0.1 cm and 0.2 cm and a value of Q which is fixed so that the constraint (3.26) is satisfied.

4. Drainpipe model

In this section we model the flow below the dip and neglect the free surface. Both the azimuthal and the vertical velocities are high in the central downflow region compared with the bulk flow velocities, and the flow below the surface dip is an intense vortex with axial flow localized to a weakly conical region with radius comparable to the radius of the drain-hole as visualized in figure 4. Experimentally we have not been able to measure the precise form of the downflow, but our measurements indicate that the velocity profile is in between a parabolic profile and a plug flow. To model the drainpipe below the surface dip we assume for simplicity a parabolic downward flow, and we make a radial expansion of the velocity components and the pressure. We assume that the expansion is valid in the viscous vortex core and we obtain a closed system of coupled ordinary differential equations by matching the inner solution to the height-independent line vortex outside the vortex core. We reduce the problem to a single first-order differential equation and describe a numerical solution modelling the bathtub vortex.

4.1. Vertical boundary layer approximation

The downward velocity with which the fluid leaves the drain-hole is an important scale for the velocity field in the central region of the bathtub vortex. In the following we use W to denote the characteristic value of the downward velocity, Ω_C to denote the central rotation rate, and H to denote the unperturbed fluid depth. The central azimuthal velocities are large compared with the radial velocities, and we therefore approximate the radial Navier–Stokes equation using a vertical boundary layer approximation. The approximation is valid if the assumption of a small central Rossby number is satisfied

$$Ro_C = \frac{W}{H\Omega_C} \ll 1. \quad (4.1)$$

We estimate Ω_C as in equation (2.1) by matching the line vortex flow (3.16) to a rigidly rotating vortex core with radius, R_0 , equal to the radius of the drain-hole:

$$\Omega_C = \frac{F}{\pi \sqrt{\nu/\Omega} R_0^2}. \quad (4.2)$$

We find $\Omega_C \approx 10^4$ r.p.m. and $Ro_C \approx 0.01$ using the measured circulation at 12 r.p.m. (see table 1), and we therefore estimate that the assumption (4.1) is satisfied. The vertical boundary layer approximation of the central region of the bathtub vortex is

$$\frac{v^2}{r} = \frac{1}{\rho} \frac{\partial p}{\partial r}, \quad (4.3)$$

$$u \frac{\partial v}{\partial r} + w \frac{\partial v}{\partial z} + \frac{uv}{r} = v \left(\frac{\partial^2 v}{\partial r^2} + \frac{1}{r} \frac{\partial v}{\partial r} - \frac{v}{r^2} \right), \quad (4.4)$$

$$u \frac{\partial w}{\partial r} + w \frac{\partial w}{\partial z} = -\frac{1}{\rho} \frac{\partial p}{\partial z} + v \left(\frac{\partial^2 w}{\partial r^2} + \frac{1}{r} \frac{\partial w}{\partial r} \right) - g, \quad (4.5)$$

and in addition we have the continuity equation

$$\frac{1}{r} \frac{\partial(ru)}{\partial r} + \frac{\partial w}{\partial z} = 0. \quad (4.6)$$

Here and in §5 we write the Navier–Stokes equations in the laboratory reference frame, and we use p to denote the pressure and not the effective pressure as in §3.

4.2. Radial expansion

We assume that the downward flow has a parabolic profile, and in the following we expand the velocity and the pressure in powers of r . We write the expansion of w using the functions $a(z)$ and $b(z)$, the expansion of v using the functions $\Omega_1(z)$ and $\Omega_3(z)$, and the expansion of p using the functions $p_0(z)$ and $p_2(z)$:

$$u(r, z) = \frac{1}{2} a'(z) r - \frac{1}{4} b'(z) r^3, \quad (4.7)$$

$$v(r, z) = \Omega_1(z) r + \Omega_3(z) r^3, \quad (4.8)$$

$$w(r, z) = -a(z) + b(z) r^2, \quad (4.9)$$

$$p(r, z) = \rho [p_0(z) + p_2(z) r^2], \quad (4.10)$$

where the expression for u follows from the continuity equation. Using the boundary layer equations (4.3)–(4.5) we obtain to lowest order in r the following:

$$\Omega_1^2 = 2p_2, \quad (4.11)$$

$$\Omega_1 a' - a \Omega_1' = 8\nu \Omega_3, \quad (4.12)$$

$$aa' = -p_0' + 4\nu b - g, \quad (4.13)$$

where the prime denotes differentiation with respect to z . These equations for the central vortex core are similar to the equations applied by Eggers & Brenner (2000) to model a spinning jet and the nonlinear properties of its break-up into droplets. For

a free jet the system of equations are supplemented by boundary conditions at the surface of the jet, and for the central vortex core in the present case we complete the equations by matching the central flow to the outer z -independent line vortex flow.

4.3. Matching with z -independent outer flow

The radial expansion is not valid outside the vortex core where the flow is two-dimensional and z -independent. We match the inner and the outer solution at the drainpipe boundary $r_0(z)$ which we define by the condition

$$w(r_0(z), z) = 0, \quad (4.14)$$

and we therefore have the relation

$$r_0^2(z) = \frac{a(z)}{b(z)}. \quad (4.15)$$

At the drainpipe boundary we require that the velocity and the pressure are continuous. Outside the central downflow region the Ekman layer gives rise to a weak upflow and leads to a z -independent radial inflow. To satisfy the continuity equation we have

$$\frac{1}{2} a'(z) r_0(z) - \frac{1}{4} b'(z) r_0^3(z) = -\frac{q}{2\pi r_0(z)}, \quad (4.16)$$

where q is the radial flow rate per height through the drainpipe boundary. Similarly the azimuthal velocity of the inner solution is required to match the outer line vortex at the drainpipe boundary:

$$\Omega_1(z) r_0(z) + \Omega_3(z) r_0^3(z) = \frac{\Gamma}{2\pi r_0(z)}, \quad (4.17)$$

and the pressure is required to be continuous at the drainpipe boundary:

$$p_0(z) + p_2(z) r_0^2(z) = g(H - z) - \frac{\Gamma^2}{8\pi^2 r_0^2(z)}. \quad (4.18)$$

All in all we have six unknown functions, the three governing equations (4.11)–(4.13), and the three matching conditions (4.16)–(4.18). We eliminate Ω_3 , p_0 , and p_2 , and reduce the model to the three equations

$$a \Omega_1' - \left(\frac{8vb}{a} + a' \right) \Omega_1 + \frac{4v\Gamma b^2}{\pi a^2} = 0, \quad (4.19)$$

$$(a^2)' - 8vb - \frac{\Gamma^2}{4\pi^2} \left(\frac{b}{a} \right)' - \left(\frac{\Omega_1^2 a}{b} \right)' = 0, \quad (4.20)$$

$$\frac{1}{2} a' \frac{a}{b} - \frac{1}{4} b' \left(\frac{a}{b} \right)^2 = -\frac{q}{2\pi}. \quad (4.21)$$

4.4. The central swirl parameter

The three ordinary differential equations form a complete system of equations, which can be reduced to a single first-order differential equation. The first step in deriving this result is to rewrite the continuity equation (4.21) in the form

$$\left(\frac{a^2}{b} \right)' = -\frac{2}{\pi} q. \quad (4.22)$$

We integrate the equation directly and obtain

$$\frac{a^2}{b} = \frac{2}{\pi} \left[T + Q \left(1 - \frac{z}{H} \right) \right], \tag{4.23}$$

where H is the central depth of the fluid, $Q \equiv Hq$ the radial flow rate through the drainpipe boundary, and T a constant of integration which models the flow-rate supplied by the region above the drainpipe, including the top surface layer.

An increase in the central downflow velocity a is associated with an increase in the central rotation rate Ω_1 due to vortex stretching. Equation (4.19) can be rewritten

$$a^2 \left(\frac{\Omega_1}{a} \right)' - 8\nu \left(\frac{b \Omega_1}{a} - \frac{\Gamma b^2}{2\pi a^2} \right) = 0, \tag{4.24}$$

and we thus observe that the central swirl parameter Ω_1/a is conserved if the viscous term is neglected. Equation (4.24) is identical to the linear first order differential equation

$$\left(\frac{\Omega_1}{a} \right)' - 8\nu \left(\frac{b}{a^2} \frac{\Omega_1}{a} - \frac{\Gamma b^2}{2\pi a^4} \right) = 0, \tag{4.25}$$

which we solve analytically using the expression for the flow rate (4.23). We thus reduce the three first-order equations to a single first-order differential equation by integrating both the matching condition for the radial velocity and the azimuthal equation analytically. For $q \neq 0$ and $q \neq 4\pi\nu$ we find the general solution

$$\frac{\Omega_1}{a} = \frac{\Gamma}{4 [T + Q(1 - z/H)](1 - Re_r)} + C_1 \left[T + Q \left(1 - \frac{z}{H} \right) \right]^{-1/Re_r}, \tag{4.26}$$

where C_1 is an integration constant linked to the boundary condition $\Omega_1(0)$ by

$$\Omega_1(0) = \frac{1}{R_0^2} \left[\frac{\Gamma}{2\pi(1 - Re_r)} + \frac{2C_1}{\pi} (Q + T)^{1-1/Re_r} \right], \tag{4.27}$$

and where we define the radial Reynolds number $Re_r = q/4\pi\nu$.

4.5. Numerical solution of the axial equation

We rewrite the axial equation (4.20) as an equation for a alone using the analytic results for the flow-rate, a^2/b , and the central swirl parameter, Ω_1/a . We change variables from z to $y = T + Q(1 - z/H)$, and for $Re_r \neq 0$ and $Re_r \neq 1$ we obtain the equation

$$(a^2)' + \frac{a^2}{Re_r y} - \frac{\Gamma^2}{8\pi} \left(\frac{a}{y} \right)' - \frac{2}{\pi} \left[\left[\frac{\Gamma}{4(1 - Re_r)y} + C_1 y^{-1/Re_r} \right]^2 y a \right]' = 0, \tag{4.28}$$

where the derivatives are taken with respect to y . The boundary conditions for $a(z)$ and $b(z)$ at $z = 0$ are given in terms of the drain-hole radius and the total flow-rate

$$\frac{a(z=0)}{b(z=0)} = R_0^2, \quad \frac{a^2(z=0)}{b(z=0)} = \frac{2}{\pi} (T + Q), \tag{4.29}$$

and we therefore have the boundary condition

$$a(z=0) = \frac{2(T + Q)}{\pi R_0^2}. \tag{4.30}$$

Figure 10 shows a typical numerical solution of the drainpipe model (4.28). The axial velocity functions a and b are approximately linear in a large z -range, whereas the

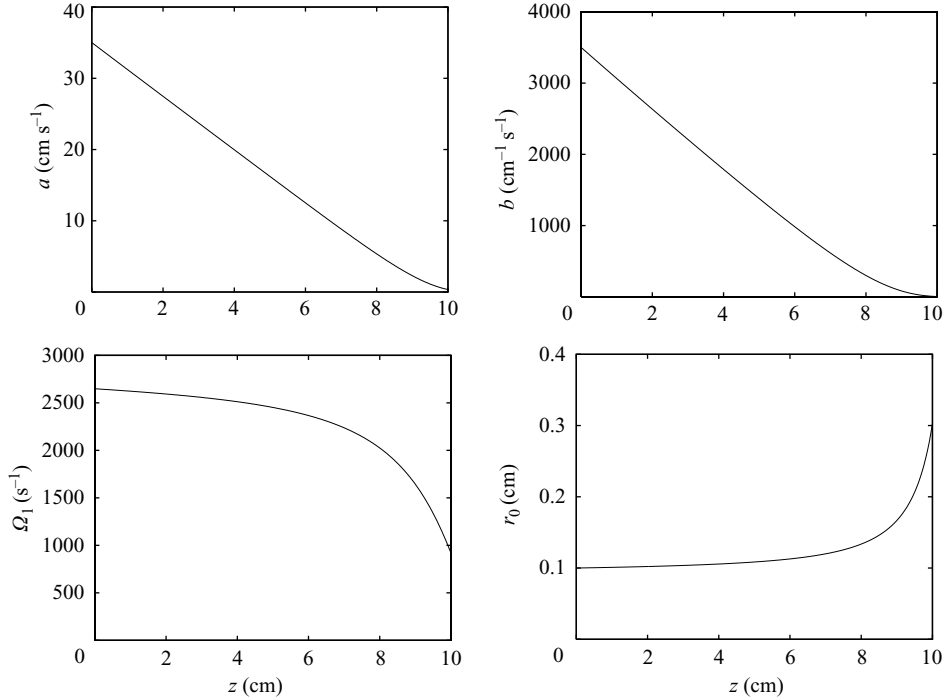


FIGURE 10. Numerical solution of equation (4.28) with $R_0 = 0.1$ cm, $H = 10.0$ cm, $\Gamma/2\pi = 15.0$ cm² s⁻¹, $\nu = 0.01$ cm² s⁻¹, $Q = 0.5$ cm³ s⁻¹, $T = 0.05$ cm³ s⁻¹, and $C_1 = 1.0$ in CGS units. The parameters give $Re_r = 5/4\pi \approx 0.4$. The axial velocity functions a and b , the angular velocity Ω_1 , and the drainpipe radius r_0 are shown as functions of z .

angular velocity Ω_1 varies slowly and is almost constant in the same z -range. The drainpipe radius r_0 is similarly almost constant except at the top where the drainpipe expands.

5. Lundgren's model

To model the free surface of the bathtub vortex we need equations which include the free-surface height and satisfy the kinematic and the dynamical boundary condition at the free surface. In the following we outline the model developed by Lundgren (1985) of the free surface bathtub vortex in a rotating cylindrical container with a drain-hole. Lundgren derived a system of two coupled ordinary differential equations for the azimuthal velocity and the surface height under the assumption of a small central downflow velocity

$$W^2 \ll 2gH, \quad (5.1)$$

and a small global Rossby number

$$Ro_G = \frac{W}{H\Omega} \ll 1, \quad (5.2)$$

see Lundgren (1985) equations (4.1), (4.15), and (4.18). In the bathtub vortex experiment we have $Ro_G \approx 10$, and do not satisfy equation (5.2). However, we have $Ro_C \approx 0.01$ (see table 1), and we satisfy the weaker but sufficient condition (4.1). Lundgren's approximation of the radial equation (4.3) is therefore applicable even

though the original assumption (5.2) is not satisfied. The outflow in the experiment is driven by gravity, and we thus have that $W \approx \sqrt{2gH}$ from Torricelli's theorem. The assumption of a small central downflow velocity (5.1) is thus not satisfied in the experiment, and we should expect corrections to the hydrostatic pressure. However, the vertical velocities close to the free surface are considerably smaller than the free-fall velocity at the drain-hole, since there is a stagnation point at the tip and the vertical velocity increases downward.

5.1. Governing equations and boundary conditions

We assume that the central Rossby number is small, see equation (4.1), and apply the vertical boundary layer approximation (4.3)–(4.5) to model the central free-surface vortex flow. The flow is required to satisfy the kinematic boundary condition at the free surface which expresses that the flow is parallel to the surface:

$$\frac{dh}{dr} = \frac{w}{u} \quad \text{at } z = h(r), \quad (5.3)$$

where we use $h(r)$ to denote the height of the free surface. There is also a dynamical boundary condition at the free surface which expresses that the force terms at the surface must balance the pressure force from the air which acts perpendicular to the surface (Batchelor 1967). In this section we neglect the viscous terms in the dynamical boundary condition, and we only require that the pressure condition is satisfied.

5.2. Lundgren's differential equations

The axial Navier–Stokes equation (4.5) simplifies considerably if the downward velocities are small compared with the free-fall velocity, i.e. if the condition (5.1) is satisfied. The assumption that the downflow velocity at the drain-hole is small in comparison with the free-fall velocity is not satisfied in the experiment, but the vertical velocities close to the free surface are considerably smaller than the free-fall velocity at the drain-hole. We therefore neglect the nonlinear terms in the axial Navier–Stokes equation and in the following we shall in addition assume that the viscous terms in the axial equation are negligible. The axial equation thus reduces to

$$0 = -\frac{1}{\rho} \frac{\partial p}{\partial z} - g. \quad (5.4)$$

This equation is directly integrated and to satisfy the dynamical boundary condition at the free surface we thus obtain the standard equation for hydrostatic pressure with an additional term due to surface tension

$$p(r, z) = \rho g[h(r) - z] - \alpha \kappa(r), \quad (5.5)$$

where α is the surface tension and κ is the curvature of the surface

$$\kappa = \frac{h'}{r[1 + (h')^2]^{1/2}} + \frac{h''}{[1 + (h')^2]^{3/2}}. \quad (5.6)$$

The radial Navier–Stokes equation (4.3) therefore reduces to the balance between the hydrostatic pressure gradient, the surface tension term, and the centrifugal term

$$\frac{v^2}{r} = g \frac{dh}{dr} - \frac{\alpha}{\rho} \frac{d\kappa}{dr}. \quad (5.7)$$

This equation makes it evident that the azimuthal velocity, v , is independent of the height z and thus a function of r only. Terms like $w \partial v / \partial z$ in the azimuthal

Navier–Stokes equation (4.4) thus vanish and the equation reduces to

$$u \left(\frac{dv}{dr} + \frac{v}{r} \right) = v \left(\frac{d^2v}{dr^2} + \frac{1}{r} \frac{dv}{dr} - \frac{v}{r^2} \right), \quad (5.8)$$

from which it follows that the radial velocity is also independent of height. The three Navier–Stokes equations have thus been reduced to the two ordinary differential equations (5.7) and (5.8) which involve the three unknown functions u , v , and h .

The flow must in addition satisfy the continuity equation (4.6) and the kinematic boundary condition at the free surface (5.3). The fact that u is independent of z has the important consequence that w is linear in z . This result follows from the continuity equation (4.6) which thus can be written

$$\frac{1}{r} \frac{d(ru)}{dr} + \frac{w(z=h) - w(z=0)}{h} = 0, \quad (5.9)$$

where $w(z=0)$ and $w(z=h)$ are the vertical velocities at the bottom and at the surface, respectively. We shall take $w(z=0)$ to be the vertical velocity above the Ekman layer (3.28), and the Ekman pumping velocity thus puts an important constraint on the free surface flow above. It follows that $w(z=h)$ can be eliminated from the continuity equation using the kinematic boundary condition (5.3) and we obtain the equation

$$\frac{1}{r} \frac{d(hru)}{dr} = w(z=0). \quad (5.10)$$

The free-surface bathtub vortex is thus modelled by the three coupled ordinary differential equations (5.7), (5.8), and (5.10) supplemented by the definition of the surface curvature in equation (5.6). We obtain the product hu by using the measured vertical velocity profile (3.28) and integrating equation (5.10):

$$hu = \begin{cases} -\frac{Qr}{2\pi R^2} & \text{if } r \leq R \\ -\frac{Q(r+d)}{2\pi(R+d)r} \exp\left(-\frac{r-R}{d}\right) & \text{if } r > R. \end{cases} \quad (5.11)$$

The task is then to obtain h and v by solving the differential equations (5.7) and (5.8).

5.3. Solutions of Lundgren's model

We first disregard the last term in equation (5.7) and solve Lundgren's equations without surface tension numerically for different values of the rotation rate and compare the numerical solutions with the experimental data at 12 r.p.m. We apply the vertical velocity profile (3.28) with the length scale $d = 0.35$ cm obtained from the measured profile at 12 r.p.m., and we use the values $R = 0.17$ cm for the radius of the downflow region of the vertical velocity profile close to the bottom and the corresponding flow rate $Q = 1.76$ cm³ s⁻¹. In the numerical solutions we set $g = 981$ cm s⁻², $\rho = 1.0$ g cm⁻³, and $\nu = 0.0089$ cm² s⁻¹. Figure 11 shows numerical solutions of the differential equations at 6 r.p.m., 8 r.p.m., 10 r.p.m., and 12 r.p.m. We find theoretically that the surface depression is 0.4 cm at 6 r.p.m. and that it increases to 2.7 cm at 12 r.p.m. This result is in qualitative agreement with the measured surface profiles at 6 r.p.m. and 12 r.p.m. shown in figure 2. The azimuthal velocity increases in the central region as the rotation rate is increased and at 12 r.p.m. the azimuthal velocities in the central region reach 35 cm s⁻¹.

Figures 12(a) and 12(b) show the numerical solution without surface tension in comparison with the experimental data at 12 r.p.m. To obtain the best possible

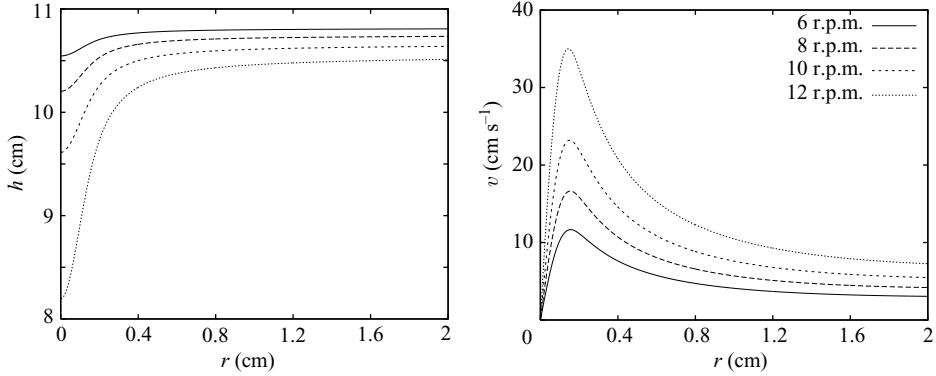


FIGURE 11. Numerical solutions of Lundgren's differential equations at rotation rates of 6 r.p.m., 8 r.p.m., 10 r.p.m., and 12 r.p.m. The surface profiles have qualitatively the same dependence on the rotation rate as the measured surface profiles at 6 r.p.m. and 12 r.p.m. shown in figure 2.

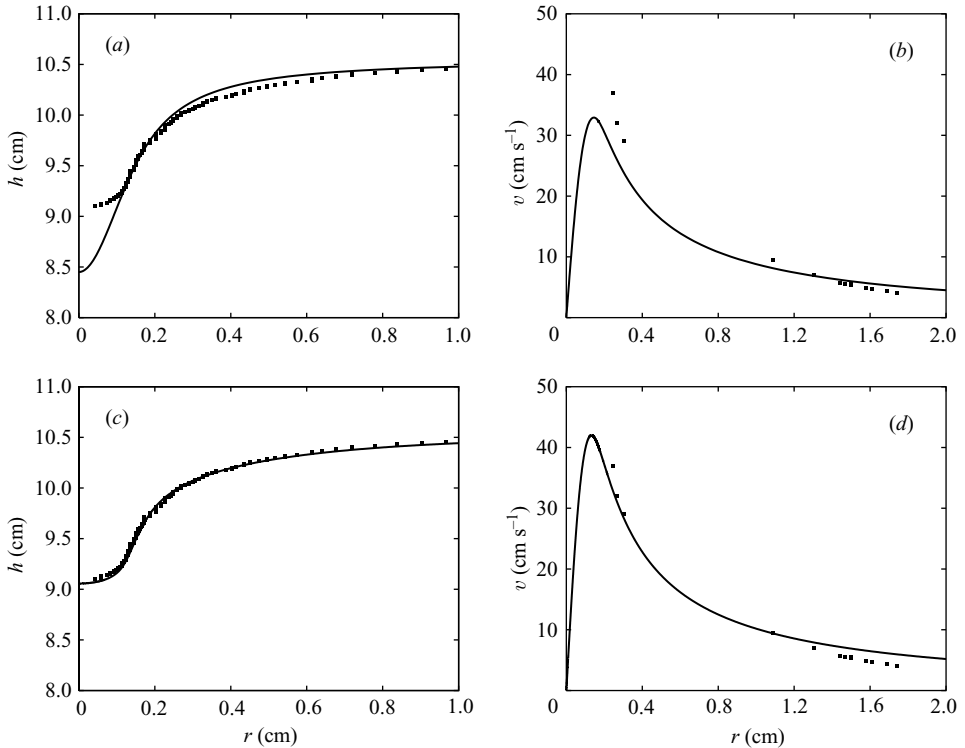


FIGURE 12. Numerical solution of Lundgren's differential equations (solid lines) and experimental data (squares) at 12 r.p.m. with h the surface height and v the azimuthal velocity in the co-rotating reference frame. The model without surface tension shown in (a) and (b) follows the measured surface profile outside the vortex core, but overestimates the depth of the central surface depression by about 1 cm. Both the surface profile and the azimuthal velocity are described well when surface tension is included as shown in (c) and (d).

agreement with the measurements we set $R=0.17$ cm and $Q=1.76$ cm³ s⁻¹. The theoretical result for the surface height follows the experimental data for $r \geq 0.2$ cm, but overestimates the depth of the central surface depression by approximately 1 cm. The numerical solution underestimates the measured azimuthal velocities by approximately 5 cm s⁻¹ in the central vortex core. There is a large difference between the measured and the theoretical surface curvature at the tip. However, an overestimate of the central surface depression and curvature is to be expected since surface tension has been neglected.

Surface tension is important since the radius of curvature of the surface is comparable with the capillary length, $l = \sqrt{\alpha/g\rho} = 0.26$ cm, obtained using the measured value of the surface tension, $\alpha = 65$ g s⁻², for the air – water interface in our experiment. By integrating the radial Navier–Stokes equation (5.7) we obtain

$$h(r) - h(0) = \frac{1}{g} \int_0^r \frac{v^2}{r'} dr' + l^2 [\kappa(r) - \kappa(0)], \quad (5.12)$$

from which it follows that the depth of the central surface depression is

$$h(\infty) - h(0) = \frac{1}{g} \int_0^\infty \frac{v^2}{r} dr - l^2 \kappa(0), \quad (5.13)$$

where we have assumed that the curvature is zero at infinity. With a given azimuthal velocity profile we thus find that the depth of the central depression is reduced due to surface tension and that the correction term is proportional to the central curvature. Based on the measured surface profile we estimate that surface tension reduces the central surface dip by approximately 1.6 cm at 12 r.p.m., and the overestimate of the depth of the central surface depression can thus be explained by the neglect of surface tension.

The differential equations for the azimuthal velocity and the surface height are more complicated to solve numerically when surface tension is included. The derivative of the curvature in equation (5.7) involves the third derivative of the surface height and the radial equation is therefore of third order in comparison with the first-order equation for the problem without surface tension. We have solved the differential equations numerically using a finite difference approach to the two-point boundary value problem. Figures 12(c) and 12(d) show the solution of Lundgren's model with surface tension effects included. To obtain the best possible agreement with the measurements we set $R=0.16$ cm and $Q=1.79$ cm³ s⁻¹. The solution with surface tension describes both the measured surface depression and azimuthal velocities well. The model with surface tension captures the curvature of the surface profile at the tip of the surface depression well, and we note that this was not possible without surface tension as shown in figure 12(a).

6. Conclusion and discussion

We have presented an experimental and theoretical investigation of the time-independent bathtub vortex in a rotating cylindrical container with a small drain-hole at the center of the bottom. Experimentally we found an intense vortex, a strong central surface depression above the drain-hole, and a complex flow structure with five characteristic flow regions as shown in figure 7, i.e. the geostrophic bulk, the bottom Ekman boundary layer, the free-surface boundary layer, the central vortex core with localized axial downflow, and the Stewartson boundary layer at the outer cylinder wall.

We found that the central vortex core is surrounded by a geostrophic bulk region with a two-dimensional line vortex flow which is independent of height, and we visualized the bottom Ekman layer which gives rise to upflow outside the central downflow region. The main part of the radial inflow takes place in the bottom Ekman layer, which thereby connects the flow rate and the strength of the line vortex as described in linear Ekman theory. We found good agreement between linear Ekman theory and our measurements, and experimentally we showed the upflow from the Ekman layer.

We modelled the central downflow region above the drain-hole with a radial expansion method in which we matched an inner viscous solution to an outer height-independent line vortex. Analytically we reduced the model to a single first-order differential equation and numerically we found that the axial velocity typically depends linearly on height whereas the azimuthal velocity is almost independent of height. The radial expansion method can be adapted to model a bathtub vortex with the free surface extending down to the drain-hole. However, the parabolic ansatz for the downflow does not allow a description of a flow with a central stagnation point on the axis of symmetry, e.g. a bathtub vortex with a finite surface depression. To model the flow close to such a point we must expand w to fourth order, $w(r, z) = -a(z) + b(z)r^2 + c(z)r^4$, and consider the governing equations to the second lowest order in r . The function a is equal to zero at the stagnation point, whereas b and c are not restricted to have any specific values there. Above the stagnation point a is negative whereas a is positive below the stagnation point where we expect that the downflow is described well by a parabolic profile. At the same time the vertical boundary layer approximation is not applicable close to the stagnation point, since the vertical and the radial velocities are comparable there. To model flows with a finite surface depression there are thus several factors which complicate the calculations, but the fourth-order downflow profile allows a description of the topology of the flow around the tip.

We applied Lundgren's model of the bathtub vortex with a free surface and compared numerical solutions of the model with our experimental data on the surface profile and the vertical and azimuthal velocities. We found that the numerical solutions were in qualitative agreement with the measurements and showed a similar dependence on the rotation rate of the container as the measured surface profiles. We discussed the importance of surface tension and showed how to include surface tension corrections in Lundgren's differential equations. We found that the measured velocities and surface profile at the intermediate rotation rate of 12 r.p.m. were well described quantitatively by the model when Ekman upflow and surface tension effects were included. We do not have measurements of the central upflow and azimuthal velocities at other values of the rotation rate, and it would be interesting to test Lundgren's model when the depth of the central surface depression is large and to investigate how the parameters Q , d , and R depend on the rotation rate. In Lundgren's model without surface tension we found that the surface depression increases with increasing rotation rate until the free surface extends to the drain-hole, whereas we were not able to solve Lundgren's equations numerically with surface tension and large surface depression. It is therefore possible that a singularity related to the bubble forming instability exists in Lundgren's equations, and this point deserves to be investigated further.

An interesting aspect of the free-surface depression, which also should be examined, is the surface tension related instability leading to formation of helical surface waves.

Helical surface waves are well-known from the time-dependent bathtub vortex in a non-rotating geometry and from the draining of a kitchen sink or a real bathtub. We were able to create helical travelling waves on the free surface in the bathtub vortex experiment by breaking rotational symmetry using a rigid rod mounted vertically in the cylindrical container close to the outer rim. The weak perturbation of the otherwise rotationally symmetric conditions lead to persistent travelling waves which were very clearly visible for states with strong surface depression, e.g. with rotation rate of 18 r.p.m. It would be interesting to study the helical wave instability further under simplified conditions and to investigate when helical waves are formed and what their characteristics are.

We thank Jens Eggers and Vachtang Putkaradze for drawing our attention to the work by Lundgren (1985) and Tom Lundgren for helpful suggestions. We also thank Morten Ernebjerg, Mark Schram Christensen, Morten Nørgaard Nielsen, and Jacob Richter for inspiration and help with a series of preparatory experiments.

REFERENCES

- ANDERSEN, A., BOHR, T., STENUM, B., JUUL RASMUSSEN, J. & LAUTRUP, B. 2003 Anatomy of a Bathtub Vortex. *Phys. Rev. Lett.* **91**, 104502.
- ANDERSEN, A., LAUTRUP, B. & BOHR, T. 2003 An averaging method for nonlinear laminar Ekman layers. *J. Fluid Mech.* **487**, 81–90; and corrigendum *J. Fluid Mech.* **493**, 379.
- BATCHELOR, G. K. 1967 *An Introduction to Fluid Dynamics*. Cambridge University Press.
- DONALDSON, C. DUP. & SULLIVAN, R. D. 1960 Behaviour of solutions of the Navier–Stokes equations for a complete class of three-dimensional viscous vortices. *Proc. Heat Transfer and Fluid Mechanics Institute, Stanford University*, p. 16.
- EGGERS, J. & BRENNER, M. P. 2000 Spinning jets. *Proc. IUTAM Symp. on Nonlinear Waves in Multi-Phase Flow*. Kluwer.
- EINSTEIN, H. A. & LI, H. 1951 Steady vortex flow in a real fluid. *Proc. Heat Transfer and Fluid Mechanics Institute, Stanford University*, pp. 33–43.
- FEYNMAN, R. P., LEIGHTON, R. B. & SANDS, M. 1965 *The Feynman Lectures on Physics*. Addison Wesley.
- GARSTECKI, P., GITLIN, I., DILUZIO, W., WHITESIDES, G. M., KUMACHEVA, E. & STONE, H. A. 2004 Formation of monodisperse bubbles in a microfluidic flow-focusing device. *Appl. Phys. Lett.* **85**, 2649–2651.
- GREENSPAN, H. P. 1968 *The Theory of Rotating Fluids*. Cambridge University Press.
- VON KÁRMÁN, T. 1921 Über laminare und turbulente Reibung. *Z. Angew. Math. Mech.* **1**, 233–252.
- KAWAKUBO, T., TSUCHIYA, Y., SUGAYA, M. & MATSUMURA, K. 1978 Formation of a vortex around a sink: A kind of phase transition in a nonequilibrium open system. *Phys. Lett. A* **68**, 65–66.
- KAYE, G. W. C. & LABY, T. H. 1973 *Tables of Physical and Chemical Constants*, 14th Edn. Longman.
- LAMB, H. 1945 *Hydrodynamics*. Dover.
- LEWELLEN, W. S. 1962 A solution for three-dimensional vortex flows with strong circulation. *J. Fluid Mech.* **14**, 420–432.
- LUGT, H. J. 1995 *Vortex Flow in Nature and Technology*. Krieger.
- LUNDGREN, T. S. 1985 The vortical flow above the drain-hole in a rotating vessel. *J. Fluid Mech.* **155**, 381–412.
- MORY, M. & YURCHENKO, N. 1993 Vortex generation by suction in a rotating tank. *Eur. J. Mech., B/Fluids* **12**, 729–747.
- OWEN, J. M., PINCOMBE, J. R. & ROGERS, R. H. 1985 source-sink flow inside a rotating cylindrical cavity. *J. Fluid Mech.* **155**, 233–265.
- PEDLEY, T. J. 1967 The stability of rotating flows with a cylindrical free surface. *J. Fluid Mech.* **30**, 127–147.

- POHLHAUSEN, K. 1921 Zur näherungsweise Integration der Differentialgleichung der laminaren Grenzschicht. *Z. Angew. Math. Mech.* **1**, 252–268.
- PONSTEIN, J. 1959 Instability of rotating cylindrical jets. *Appl. Sci. Res. A* **8**, 425–456.
- SHAPIRO, A. H. 1962 Bath-tub vortex. *Nature* **196**, 1080–1081.
- TREFETHEN, L. M., BILGER, R. W., FINK, P. T., LUXTON, R. E. & TANNER, R. I. 1965 The bath-tub vortex in the southern hemisphere. *Nature* **207**, 1084–1085.